

Suzaku monitoring of the Wolf-Rayet binary WR 140 around periastron passage: An approach for quantifying the wind parameters

Yasuharu SUGAWARA,¹ Yoshitomo MAEDA,^{2,3} Yohko TSUBOI,¹ Kenji HAMAGUCHI,^{4,5} Michael CORCORAN,^{4,5}
A. M. T. POLLOCK,^{7,8} Anthony F. J. MOFFAT,⁹ Peredur M. WILLIAMS,¹⁰ Sean DOUGHERTY,¹¹ and Julian PITTARD,¹²

¹*Department of Physics, Faculty of Science & Engineering, Chuo University, 1-13-27 Kasuga, Bunkyo, Tokyo 112-8551*

²*Institute of Space and Astronautical Science, Japan Aerospace Exploration Agency 3-1-1 Yoshinodai, Sagami-hara, Kanagawa 229-8510*

³*Department of Space and Astronautical Science, SOKENDAI (The Graduate University for Advanced Studies), 3-1-1 Yoshinodai, Chuo-ku, Sagami-hara, Kanagawa 252-5210*

⁴*CRESST and X-ray Astrophysics Laboratory NASA/GSFC, Greenbelt, MD 20771, USA*

⁵*Department of Physics, University of Maryland, Baltimore County, 1000 Hilltop Circle, Baltimore, MD 21250, USA*

⁶*Universities Space Research Association, 7178 Columbia Gateway Drive, Columbia, MD 21046, USA*

⁷*European Space Agency, XMM-Newton Science Operations Centre, European Space Astronomy Centre, Apartado 78, Villanueva de la Cañada, 28691 Madrid, Spain*

⁸*Department of Physics and Astronomy, University of Sheffield, Sheffield S3 7RH, England*

⁹*Département de Physique, Université de Montréal, Succursale Centre-Ville, Montréal, QC H3C 3J7, and Centre de Recherche en Astrophysique du Québec, Canada*

¹⁰*Institute for Astronomy, Royal Observatory, Blackford Hill, Edinburgh EH9 3HJ, Scotland*

¹¹*National Research Council of Canada, DRAO, Penticton*

¹²*School of Physics and Astronomy, The University of Leeds, Leeds LS2 9JT
sugawara@phys.chuo-u.ac.jp*

(Received 2012 May 15; accepted 2015 September 10)

Abstract

Suzaku observations of the Wolf-Rayet binary WR 140 (WC7pd+O5.5fc) were made at four different times around periastron passage in 2009 January. The spectra changed in shape and flux with the phase. As periastron approached, the column density of the low-energy absorption increased, which indicates that the emission from the wind-wind collision plasma was absorbed by the dense W-R wind. The spectra can be mostly fitted with two different components: a warm component with $k_{\text{B}}T = 0.3\text{--}0.6$ keV and a dominant hot component with $k_{\text{B}}T \sim 3$ keV. The emission measure of the dominant, hot component is not inversely proportional to the distance between the two stars. This can be explained by the O star wind colliding before it has reached its terminal velocity, leading to a reduction in its wind momentum flux. At phases closer to periastron, we discovered a cool plasma component in a recombining phase, which is less absorbed. This component may be a relic of the wind-wind collision plasma, which was cooled down by radiation, and may represent a transitional stage in dust formation.

Key words: stars: Wolf-Rayet — stars: binaries: eclipsing — stars: winds, outflows — X-rays: individual (WR 140)

1. Introduction

Mass-loss is one of the most important and uncertain parameters in the evolution of a massive star. There are several methods for determining mass-loss rates (e.g., via radio continuum flux, radiative transfer and polarization variation in close binaries). It has become increasingly recognized (e.g., Puls et al. 2006) that smooth-wind models, based on density-squared diagnostics, overestimate clumped wind mass-loss rates by up to an order of magnitude.

Another important parameter for massive stars is the wind acceleration. For most radiatively-driven stellar-wind models, a velocity law $v(r) = v_{\infty}(1 - R/r)^{\beta}$ with $\beta = 1$ is assumed. Here, v_{∞} and R are the terminal wind-velocity and stellar radius, respectively. In this model, usually the initial wind velocity v_0 is neglected, since it is thought to be $\sim 1\%$ of v_{∞} and the wind-collision X-rays are formed relatively far out in the wind. On the other hand, some optical observations have

revealed a high value of β for Wolf-Rayet (W-R) stars (e.g., $20 R_{\odot} < \beta R < 80 R_{\odot}$; Lépine & Moffat 1999, which lead to values $\beta \gg 1$ for normal W-R radii).

While the mass-loss rate and the acceleration parameter β have been measured using the radio/IR continuum flux or line spectral analysis at optical/IR wavelengths, X-ray wavelength could be an independent window to approach these parameters. Colliding wind binary is a good target, having variable X-ray spectra with orbital phase. The X-ray is emitted from the wind-shocked region, which is strongly dependent on the ram-pressure balance between the two hypersonic winds. The shocked plasmas, which have temperatures of $10^7\text{--}10^8$ K, are frequently observed, and the high absorption column of $10^{22}\text{--}10^{23}$ H cm⁻² are reported (cf. Schild et al. 2004). The temperature should reflect on the wind velocity, and the absorption column indicates the dense W-R wind (Koyama et al. 1994), i.e. mass-loss rate of the W-R star (cf. Pollock et al. 2005). The X-ray luminosity is highly dependent on the separation

Table 1. *Suzaku* Observation Log.

Obs.	Observation Start [UT]	Observation End [UT]	t_{exp}^* [ks]	$\dot{C}_{\text{XIS/FI}}^\dagger$ [cps]	$\dot{C}_{\text{XIS/BI}}^\dagger$ [cps]	$\dot{C}_{\text{HXD/PIN}}^\dagger$ [cps]	Orbital Phase ‡	D^\ddagger [AU]
A	2008-04-09 05:33:13	2008-04-09 17:20:18	21.6	2.186 ± 0.007	2.68 ± 0.01	0.024 ± 0.005	2.904	13.79
B	2008-12-12 10:27:51	2008-12-13 13:15:20	52.8	2.262 ± 0.005	2.415 ± 0.007	0.029 ± 0.003	2.989	3.12
C	2009-01-04 08:36:00	2009-01-05 10:12:18	47.3	0.661 ± 0.003	0.644 ± 0.004	0.008 ± 0.003	2.997	1.73
D	2009-01-13 12:59:45	2009-01-15 12:00:13	89.4	0.193 ± 0.001	0.178 ± 0.002	0.005 ± 0.002	3.000	1.53

* Net exposure of the XIS.

$^\dagger \dot{C}$ shows net count rate in counts per second (cps). The bandpasses are 0.4–10 keV for the FI and BI detectors and 15–50 keV for the PIN detectors.

‡ According to Monnier et al. (2011). D shows binary separation.

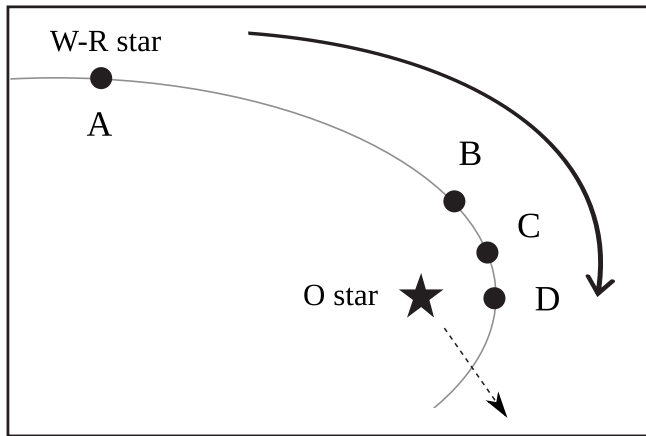


Fig. 1. Schematic view of the orbit of the WR 140 system. The filled circles show relative positions of the W-R star during observations A–D. The dashed arrow shows the line of sight to Earth.

between the stars of the binary, the mass-loss rates, and wind velocities (Stevens et al. 1992; Usov 1992). If we know the orbital parameters of the binary, the X-ray luminosity at each orbital phase should depend on the mass-loss rates and wind-acceleration parameters.

WR 140 (HD 193793) is considered as the textbook example of a colliding wind binary. The star has been classified as a WC7pd+O5.5fc binary system whose stellar masses are $M_{\text{WR}} = 16 M_{\odot}$ and $M_{\text{O}} = 41 M_{\odot}$ by the optical spectroscopic monitoring (Fahed et al. 2011). Its orbit and distance have been well determined with $P_{\text{orb}} = 2896.35$ days, $i = 119.6^\circ$, $e = 0.8964$ and $d = 1.67$ kpc by detailed IR astrometric study (Monnier et al. 2011). Radio non-thermal (synchrotron) emission from WR 140 was reported that may arise from a wind-wind collision zone (e.g., Williams et al. 1990; White & Becker 1995; Dougherty et al. 2005). Pittard & Dougherty (2006) proposed a radio, X-ray and γ -ray non-thermal emission model. In their model, there are some cases where inverse Compton emission dominates the high energy X-ray emission. Pittard & Dougherty (2006) predicted that *Suzaku* would detect such non-thermal X-ray emission.

WR 140 is a bright X-ray source (e.g., Pollock 1987; Williams et al. 1990; Zhekov & Skinner 2000; Pollock et al. 2002; Pollock et al. 2005). During the previous periastron passage, *Rossini-XTE* showed a drop in X-ray flux before periastron (Pollock et al. 2005). We pursued this via *Suzaku* monitoring

during the following periastron passage in 2009. These observations cover the energy range 0.1–20 keV.

2. Observations and Data Reduction

The *Suzaku* X-ray observatory (Mitsuda et al. 2007) is equipped with two kinds of instruments; the XRT (X-Ray Telescope, Serlemitsos et al. 2007) + XIS (X-ray Imaging Spectrometer: Koyama et al. 2007a) system, sensitive to X-rays between 0.3–12 keV, and the HXD (Hard X-ray Detector: Kokubun et al. 2007; Takahashi et al. 2007) sensitive to X-rays above 10 keV. *Suzaku* observed WR 140 four times around periastron passage in 2009 January. Sequence numbers of the data are 403030010, 403031010, 403032010 and 403033010. Logs of these four observations, labeled as A, B, C and D, are summarized in table 1 and figure 1. The total exposure of these observation was ~ 210 ks.

The XIS is composed of four X-ray CCD (XIS0–3) arrays with 1024×1024 pixel formats, each of which is mounted at the focal plane of an individual XRT. The XRT+XIS system covers a field of view of $\sim 18' \times 18'$. The XIS1 has a back-side illuminated (BI) CCD chip while the remaining active sensors (XIS0 and XIS3) have front-side illuminated (FI) chips. The BI and FI chips are superior to each other in the soft and hard band responses respectively. During the observations, the XISs were operated in the normal clocking mode with the default frame time (8 s). WR 140 was placed at the HXD nominal position.

The HXD is a non-imaging instrument that consists of a 4×4 array of detectors (well units) and 20 surrounding crystal scintillators for active shielding. Each well unit consists of four Si PIN diodes (PIN), sensitive to X-rays between 10–70 keV, and four GSO/BGO phoswich counters (GSO) for detecting photons with energies in the range 40–600 keV. We used only PIN data to constrain the emission above 10 keV due to the high background of the GSO instrument.

We reduced the data using HEASOFT¹ version 6.16.0 and calibration versions (CALDBVER) xis20090402, xrt20080709 and hxd20090402. We screened out XIS and HXD events obtained during (1) the South Atlantic Anomaly (SAA) passage, (2) the low geomagnetic cut-off rigidity (6 GV for the XIS and 8 GV for the HXD), (3) low elevation angles from the Earth rim ($< 10^\circ$ for the XIS and $< 5^\circ$ for the HXD) and the sun-lit Earth rim ($< 20^\circ$), and (4) telemetry saturation. We used XSPEC² version 12.5.1 for spectral analysis.

¹ <http://heasarc.gsfc.nasa.gov/docs/software/lheasoft/>

² <http://heasarc.gsfc.nasa.gov/xanadu/xspec/>

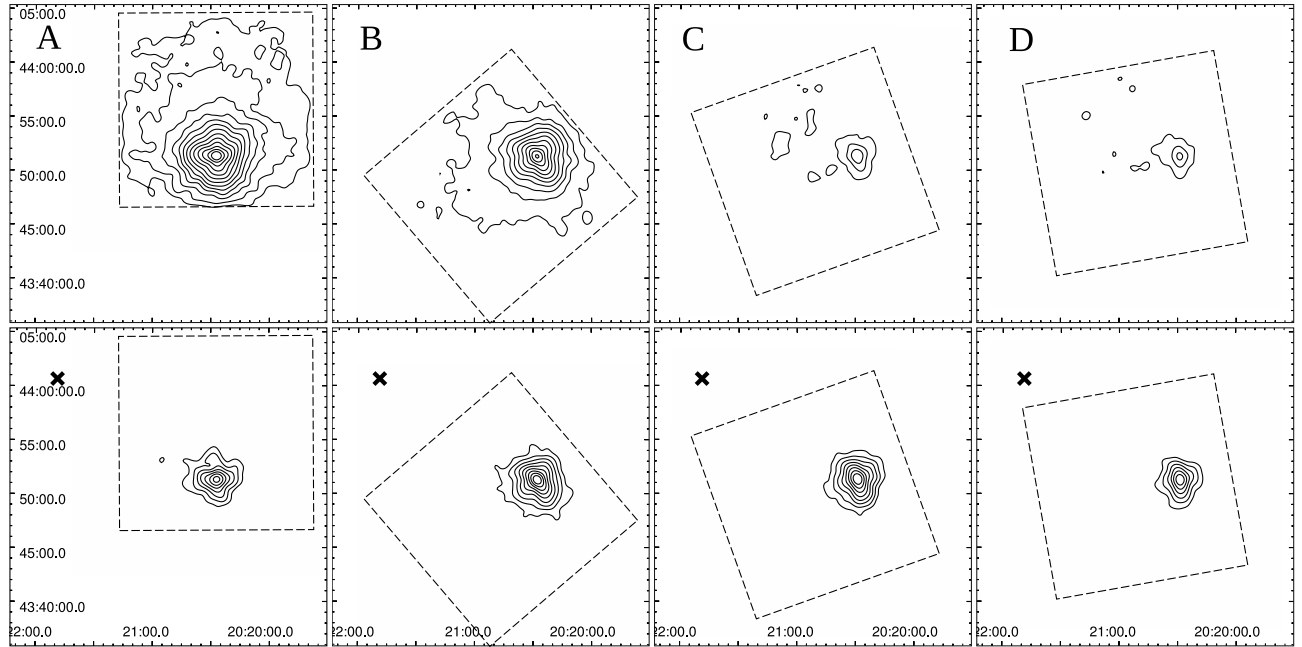


Fig. 2. *Suzaku* XIS (0+1+3) contour images of WR 140. Top panels: 0.4–1.6 keV band. Bottom panels: 7–10 keV band. The contour levels are for soft band, 0.04, 0.08, 0.16, 0.32, 0.64, 1.28, 2.56, 5.12, 10.24, 20.48, 40.96, 81.92 and for hard band, 0.025, 0.04, 0.064, 0.102, 0.164, 0.262, 0.419, 0.671, 1.074 in units of counts ks^{-1} pixel^{-1} . In the soft band images of the observation C and D, some weak sources are located in the west region of WR 140. Since the flux of these sources varied between observations C and D, they are considered as the variable point sources. The dashed lines show the XIS field of view. The crosses show the location of IGR J20216+4359.

3. Data Analysis and Results

3.1. Spectral Characteristics

Figure 2 shows the XIS images in the soft (0.4–1.6 keV) band and the hard (7–10 keV) band. In all the observations, the XISs detected an X-ray source at the position of WR 140. In order to capture the spectral characteristics of WR 140, we extracted the source events from a circle with 4 arcmin radius centered on the X-ray peak, which gives a maximum signal-to-noise ratio in the 0.4–10 keV band. We extracted background events from the entire XIS field of view, excluding the region within 5 arcmin from the X-ray peak and calibration source regions. WR 140 did not show any significant X-ray variation during each observation, so that we generated time-averaged spectra for each observation. We generated XIS detector responses (RMF) and XRT effective area tables (ARF) with `xisrmfgen` and `xissimarfgen` (Ishisaki et al. 2007) and averaged two FI spectra and responses with the `HEASOFT` `mathpha`, `addrmf` and `addarf`. The FI spectra of observations A and B, C, D were grouped to a minimum of 100 and 200 counts per bin with `FTOOL` `grppha`, respectively. Similarly, the BI spectra of observations A, B, C and D were grouped to a minimum of 100, 200, 150 and 200 counts per bin, respectively. In spectral fits, we ignored XIS bins around the Si K-edge between 1.8–2.0 keV because of the calibration uncertainty.

We noticed that the O-Ly α , Ne-Ly α and Mg-Ly α lines in the BI spectra of observations A and B deviate significantly from those lines in the Astrophysical Plasma Emission Database

(APED)³. The FI spectra did not show such deviation, and are consistent within ~ 5 eV with the values in the database. This is suggesting that the energy gain of the BI chip is not calibrated sufficiently. Center energies of these lines, measured with fits by Gaussian functions, deviate by -5 ± 3 eV and -20 ± 3 eV for observations A and B, respectively. We therefore offset those spectra by the best-fit values. We did not make gain offsets for the spectra of observations C and D, since they did not show those emission lines.

We subtracted from the pipeline-processed HXD/PIN spectra non-X-ray background (NXB) simulated with the tuned NXB model (LCFITDT, Fukazawa et al. 2009) and the typical Cosmic X-ray Background (CXB) measured with the *HEAO-1* (Boldt 1987)⁴. We generated the PIN detector response with `hxdarfgen`. The PIN spectra also were binned with `grppha`⁵.

The XIS spectra of WR 140 (figure 3) show emission lines from highly ionized ions of neon, magnesium, silicon, sulfur and iron. Earlier observations of WR 140 (*Ginga*: Koyama et al. 1990, *ASCA*: Koyama et al. 1994; Zhekov & Skinner 2000, *Chandra*: Pollock et al. 2005, *XMM-Newton*: De Becker et al. 2011) also found these lines in the spectra, suggesting optically thin plasma thermalized by wind-wind collision. The low energy cut-off — the signature of absorption by neutral matter or weakly ionized plasma — drastically increased from obser-

³ See <http://www.atomdb.org/> for details.

⁴ See http://heasarc.gsfc.nasa.gov/docs/suzaku/analysis/pin_cxb.html

⁵ Observation A: group 0 35 6 36 71 12 72 101 30 102 236 45 237 255 19;
Observation B: group 0 59 6 60 71 12 72 146 75 147 236 45 237 255 19;
Observation C: group 0 47 6 48 59 12 60 146 87 147 236 90 237 255 19;
Observation D: group 0 59 6 60 146 87 147 236 45 237 255 19

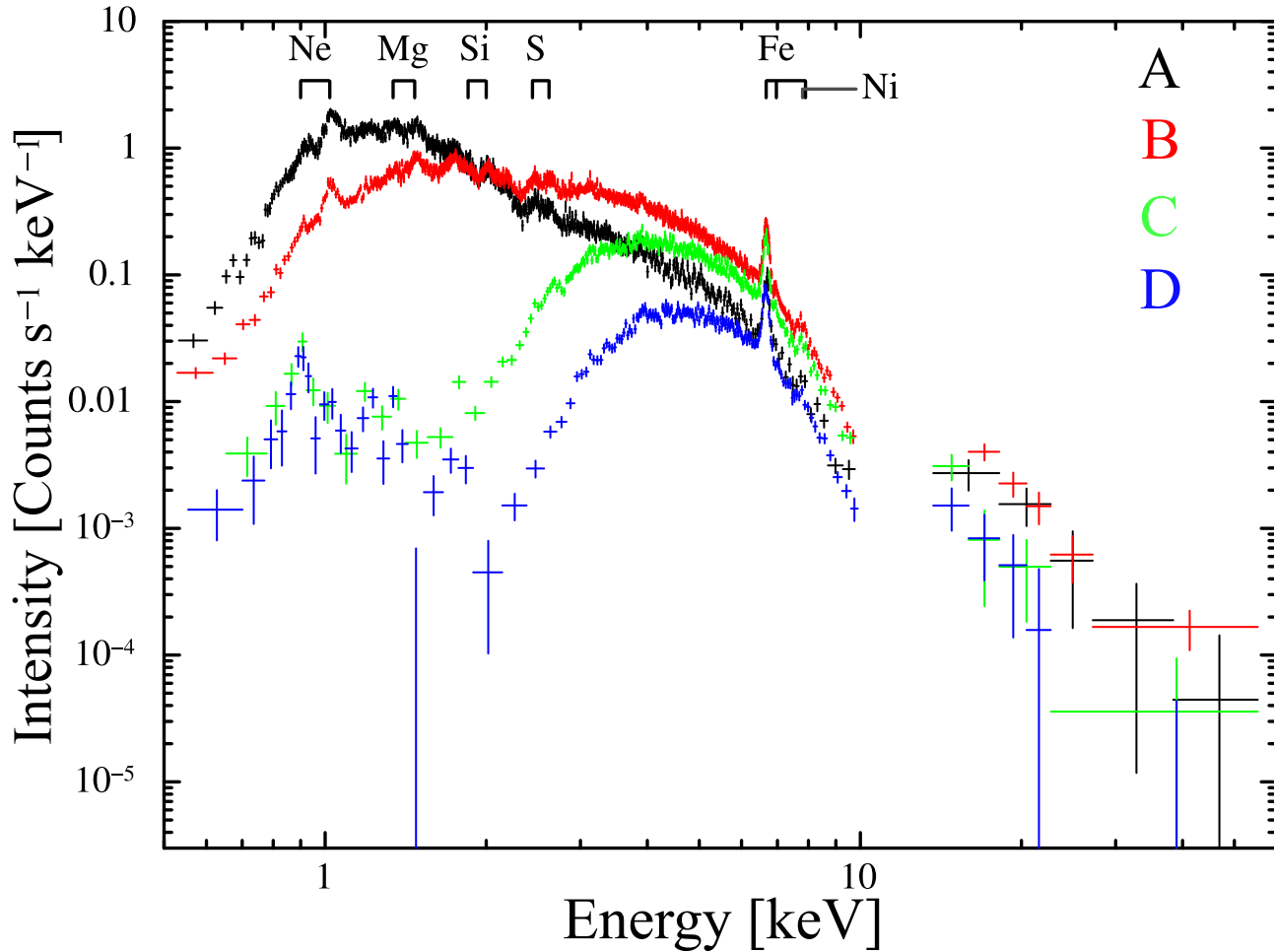


Fig. 3. Background subtracted XIS/FI and HXD/PIN spectra of WR 140.

variation A to D. High density and/or large atomic number are needed for large absorption. In WR 140, the mass-loss rate of the O-star is an order of magnitude smaller than that of the W-R star. In addition, the W-R wind have higher metal abundances than the O-star wind. Therefore, it is well known that the absorption by the W-R star is dominant (e.g., Koyama et al. 1994). The spectral variation like this was reported by Zhekov & Skinner (2000). We call this dominant emission “variable component” (see § 3.3). During observations C and D when soft X-rays from the wind-wind collision are suppressed by absorption from the wind of the W-R star, we detected another emission component below 2 keV. This component did not change apparently between these observations. We call this soft emission “cool component” (see § 3.2).

The HXD/PIN detected significant X-ray emission in the 15–50 keV range. The flux seems to change from observation B to D (see figure 3), which seems to correlate with the variation below 10 keV. However, we should pay attention to other hard X-ray source IGR J20216+4359, which is located at 17.35 arcmin away from WR 140 (Bikmaev et al. 2008). The location is shown in figure 2 & 4. Because of a potential for the contamination from IGR J20216+4359 in the field of view of PIN/HXD, XIS and PIN spectra are analyzed separately.

3.2. Cool Component

We found the cool component in the spectra of observations C and D (see § 3.1). In this subsection, we report the analysis results of the cool component. First, we check the spatial structure of the cool component. Then, we compare the spectral features of diffuse emission around WR 140 and the cool component. Finally, we fit the spectra of the cool component.

3.2.1. Radial extent of the cool component

WR 140 is located in the Cygnus region that is pervaded by diffuse X-ray emission from a large ring-like structure, whose diameter is $\approx 13^\circ$. This diffuse structure is known as the Cygnus superbubble (CSB). We then figure out the spatial structure of the cool component before the spectral analysis.

Figure 4 shows *Suzaku* images in the 0.4–1.6 keV and 7–10 keV band, combined from observations C and D. In the soft band, the diffuse emission with some degree of inhomogeneity is seen. The north and east areas were brighter than the south area by a factor of two in count rate. Some transient sources were identified in observations C and D.

Figure 5 shows the radial profiles of the *Suzaku* XIS images for observation D. The images are taken with XIS-0, 1, and 3, and summed up. In figure 5, the dashed line in each panel shows the background level determined by the fitting of the

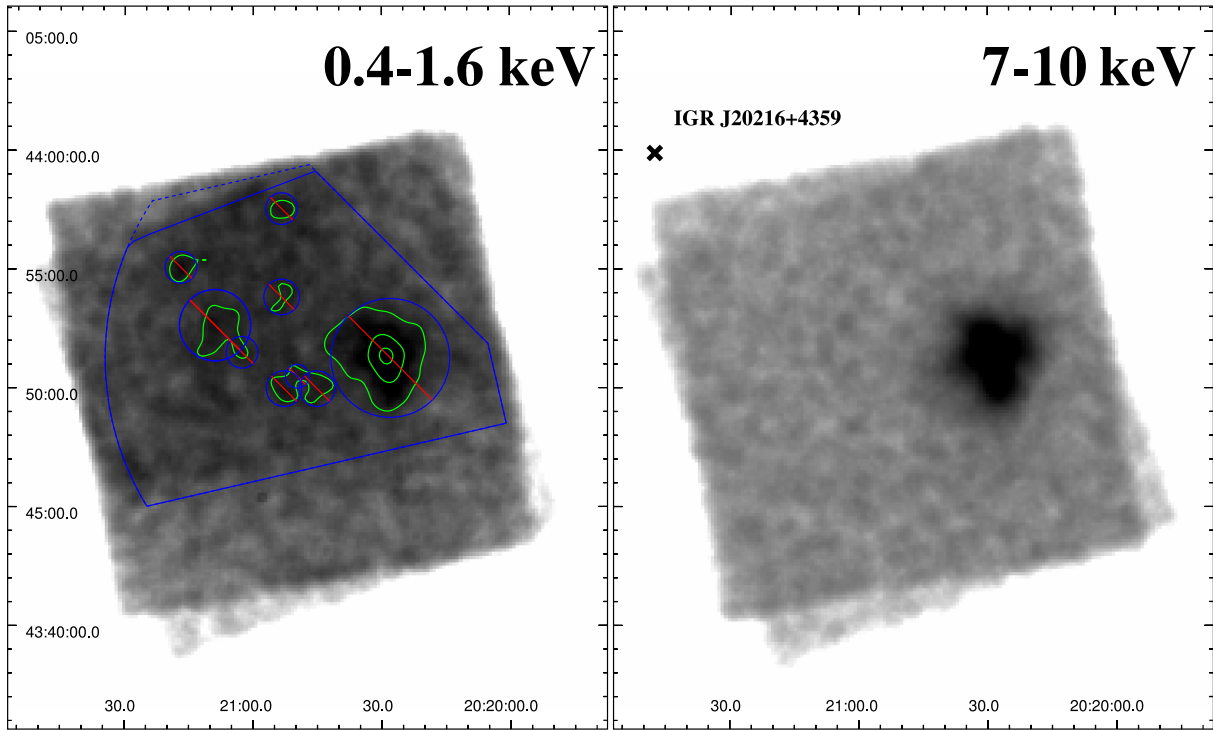


Fig. 4. *Suzaku* XIS (0+1+3) images with a log color scale obtained at observations C and D. We averaged the images of observations C and D. Left panel shows 0.4–1.6 keV band, and right panel shows 7–10 keV band. Images have been smoothed with a Gaussian function with $\sigma = 2.5$ image pixels (~ 21 arcsec). The contour levels are 0.039, 0.073, 0.138 in units of counts $\text{ks}^{-1} \text{pixel}^{-1}$. We used the arc region as the background of the cool component excluding nine circle areas (see the text for the detail). The solid and dashed outer lines show the background regions for observation C and D, respectively. The XIS has a spatial resolution of about 2 arcmin in a half-power diameter.

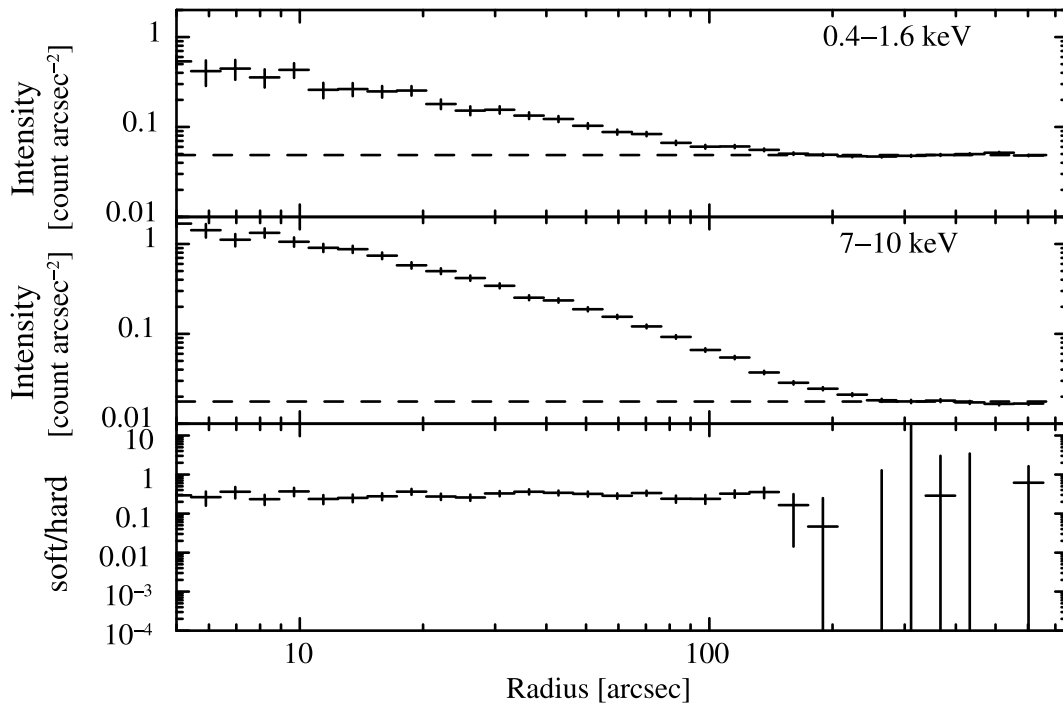


Fig. 5. Radial profiles which are centered on WR 140. The data are summed up for XIS-0, 1 and 3. Only observation D is used. Top: 0.4–1.6 keV (soft). Center: 7–10 keV (hard). Dashed lines show the count rates of our assumed background level that consists of the Cygnus superbubble and the NXB. Bottom: The ratio of the soft to the hard energy-band data after the constant background is subtracted.

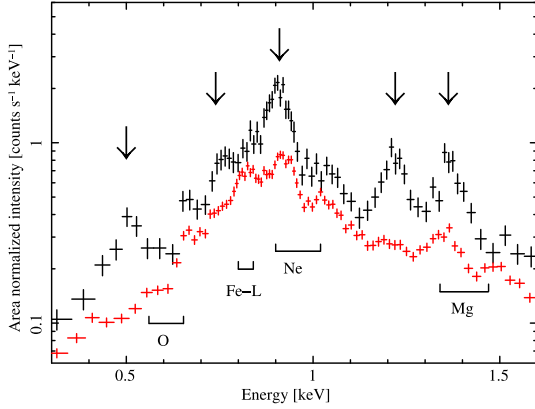


Fig. 6. Comparison of the spectra of the source (black) and background (red) regions. The data of XIS-0, 1 and 3 for observations C and D were summed to make the spectra. Downward-pointing arrows indicate prominent excess of the source spectrum over the background.

data between 200–600 arcsec from WR 140 with a constant model. The bottom panel in figure 5 shows the ratio of the soft band count rate and the hard band count rate, after background subtraction. The ratio is nearly flat along the radial axis. The point spread functions of the XISs do not significantly show the energy dependency (Serlemitsos et al. 2007). Since the emission from the point source WR 140 dominated the XIS count rate in the hard band, the constant ratio indicates that the cool component is also point-like and associated with WR 140.

3.2.2. Spectral features

In this subsection, we compare the spectral features of the background diffuse emission around WR 140 and the cool component. Since WR 140 lies in the north area of the diffuse structure, we adopted the north and east regions of WR 140 as the background region for observations C and D. We excluded the transient sources from the background region, as shown in figure 4. In order to improve the signal-to-noise ratio of the spectra in the 0.4–1.6 keV band, we extracted source events within 2 arcmin from the X-ray peak. We co-added the XIS-0, 1 and 3 spectra for observations C and D and ignored spectral bins above 1.6 keV.

Figure 6 shows the area-normalized spectra of the source and the background region. NXB subtraction were not made for both of the spectra. The spectra of the background region was fairly complex, which had O-Ly α , Ne-Ly α and Mg-Ly α lines and the structures of He-like O and Ne. On the other hand, the source spectrum shows large excess from the background. Especially, the structures, which are shown with arrows in figure 6, are unique to the source spectrum, and cannot be made by an inappropriate background subtraction. At least the 1.2 keV peaked structure in these unique structures could not be reproduced by collisional equilibrium (CE) plasma model. The detail is discussed in § 3.2.3.

The observed surface brightness of background region was 4×10^{-14} erg s $^{-1}$ cm $^{-2}$ arcmin $^{-2}$ (0.5–2 keV). This value was obtained from a fit of the NXB subtracted BI spectrum for observation D by a thin thermal plasma model (APEC: Smith et al. 2001). We adopted the ancillary response file for a circular flat field sky with a 20 arcmin radius. This observed surface

Table 2. Results of spectral fitting for cool component.

Components	Parameters	
Absorption	$N_{\text{H}}^{\text{cool}}$ (10^{21} cm $^{-2}$)	$3.8_{-1.7}^{+2.0}$
vrnei	$k_{\text{B}}T^{\text{cool}*}$ (keV)	$0.021_{-0.005}^{+0.006}$
	$k_{\text{B}}T_{\text{init}}^{\text{cool}\dagger}$ (keV)	>0.58
	N (solar)	<47
	O (solar)	$9.1_{-4.6}^{+7.0}$
	Ne (solar)	$17.1_{-11.5}^{+24.1}$
	Mg (solar)	$3.4_{-3.2}^{+7.4}$
	$\tau_{\text{u}}^{\ddagger}$ (10^{11} s cm $^{-3}$)	$2.3_{-0.5}^{+0.7}$
	norm § (10^{-5})	7.5 ± 0.7
	F_{X}^{\parallel} (10^{-13} erg cm $^{-2}$ s $^{-1}$)	1.1
	$L_{\text{X}}^{\#}$ (10^{32} erg s $^{-1}$)	2.0
	χ^2/dof	98/83

Notes. We used the spectra of observations C and D, by averaging them. We did a simultaneous fitting of the FI and BI spectra. We adopted the model TBabs * vrnei. The best-fit model is shown in figure 7 right panel with a solid line. Errors quoted are the 90% confidence interval.

* Plasma temperature

† Initial plasma temperature

‡ Ionization timescale.

§ Normalization constant defined as $E.M. \times 10^{-14} (4\pi d^2)^{-1}$, where $E.M.$ is the emission measure in cm $^{-3}$ and d is the distance in cm.

∥ The observed flux (0.4–1.6 keV)

The absorption-corrected luminosity (0.4–1.6 keV), which we calculated by assuming a distance of 1.67 kpc.

brightness is not inconsistent with the reported flux within an order of magnitude (Zhekov & Skinner 2000).

3.2.3. Spectral fitting

In this subsection, we fit the spectra of the cool component in the 0.4–1.6 keV band with two models. First, we fitted the FI and BI background subtracted spectra using a model of a one-temperature CE plasma (vAPEC) emission suffering absorption by cold matter with the interstellar medium (ISM) abundances (TBabs: Wilms et al. 2000). As for the CE plasma, the elemental abundance were fixed at the best-fit values for the variable component (see § 3.3.1 and table 3) except for N, Ne and Mg. The fitting result (figure 7 left) yields a plasma temperature of $k_{\text{B}}T^{\text{cool}} \sim 0.2$ keV and a column density $N_{\text{H}}^{\text{cool}} \sim 7 \times 10^{21}$ cm $^{-2}$ ($\chi^2/\text{dof} = 163/50$).

This model still leaves line-shaped residuals at 1.21 ± 0.01 keV. In the emission line database APED, the 1.21 keV line corresponds to Ne-Ly β line. However, in the CE plasma, the Ne-Ly β line flux must be weaker than the Ne-Ly α line flux at 1.02 keV. In order to get the line flux ratio of Ne-Ly α to Ly β , we fit the spectra using the Gaussian lines model with an absorption. The absorption fixed at $N_{\text{H}} = 7 \times 10^{21}$ cm $^{-2}$ derived from the fitting result of the CE plasma model. Figure 8 shows the confidence contour map of the normalizations of two Gaussian lines (Ne-Ly α and Ly β) and indicates that the residual at 1.2 keV is significant at the 3σ level. The best-fit ratio of Ly β /Ly α is about unity that is much larger than the ratio for the CE plasma, ~ 0.3 . The high Ly β /Ly α ratio is often obtained from a plasma in a recombining phase.

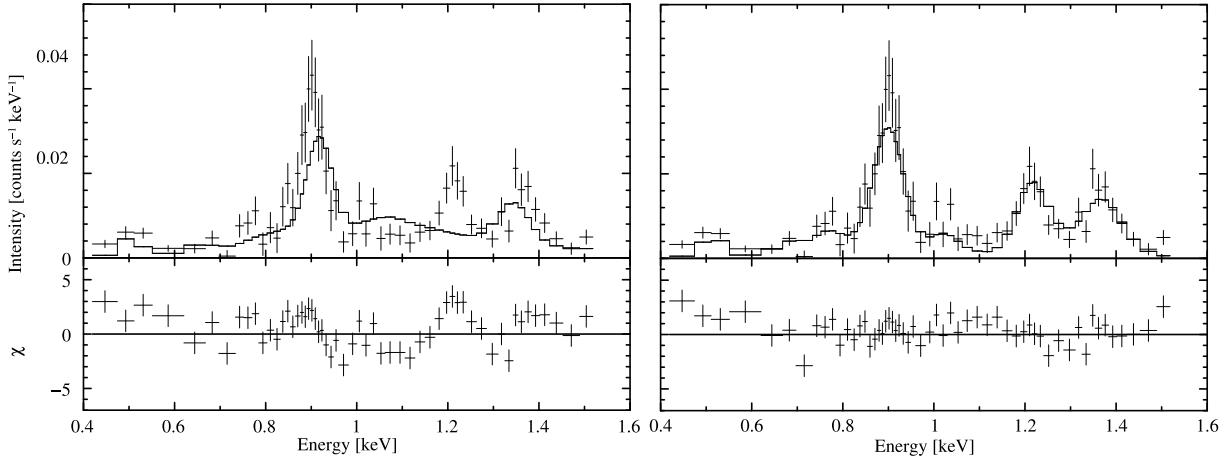


Fig. 7. The background subtracted FI spectra below 1.6 keV, where the spectra of observations C and D are averaged. The spectrum was grouped to a minimum of 40 counts per bin. *Left:* Fit with the TBabs * vAPEC model. *Right:* Fit with the TBabs * vrnei model. The solid lines show each model. The lower panels show the residuals of the data from the model. See also table 2 for the best-fit parameters.

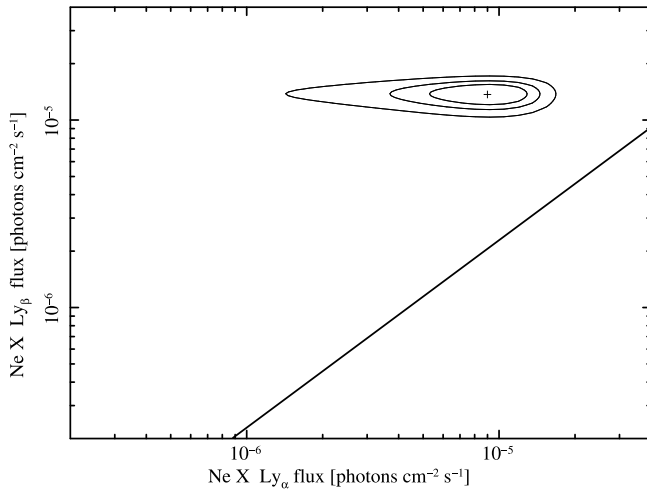


Fig. 8. The confidence contour map of the normalizations of the two Gaussian lines (Ne-Ly α and Ly β). The best-fit parameters were obtained by a simultaneous fitting of FI and BI spectra that were made by averaging the data of observations C and D. The contours are at 68%, 90%, and 99% confidence levels for two interesting parameters. The solid straight line indicates the line ratio of Ly α to Ly β , based on the APEC model.

From the above consideration, there is a possibility that the residuals at 0.5, 0.73, 0.87, 1.21 and 1.37 keV result from radiative recombination continuum (RRC) edges of C VI, O VII, O VIII, Ne IX, and Ne X, respectively. We therefore introduce non-equilibrium recombining collisional plasma model (vrnei⁶). This model is based on the assumption that the plasma changes from the collisional equilibrium state, with the initial temperature $k_B T_{\text{init}}^{\text{cool}}$, to the non-equilibrium recombining state, with the temperature $k_B T^{\text{cool}}$. The elemental abundances except for N, O, Ne and Mg were fixed at the best-fit values for the colliding wind emission (see § 3.3.1 and table 3). The reduced χ^2 was significantly improved. The best-fit results are shown in table 2. The temperature $k_B T^{\text{cool}}$ is as low

⁶ See <http://heasarc.gsfc.nasa.gov/xanadu/xspec/manual/XSmodelRnei.html>

Table 3. The best-fit values of the elemental abundance ratios of the variable components (warm and hot components) and their absorption components by number relative to helium.

Element	Abundance ratio*
He	1 ^f
C	0.4 ^f
N	0 ^f
O	7.2×10^{-2f}
Ne	$(6.0 \pm 0.2) \times 10^{-3}$
Mg	$(5.4 \pm 0.3) \times 10^{-4}$
Si	5.9×10^{-4f}
S	2.4×10^{-4f}
Ar	5.3×10^{-5f}
Ca	3.2×10^{-5f}
Fe	$(4.16^{+0.08}_{-0.14}) \times 10^{-4}$
Ni	$(1.73^{+0.03}_{-0.06}) \times 10^{-5}$

Notes. This result is obtained with the same fitting as that done to obtain the results in table 4 (observations A and B); we simultaneously fitted the FI and BI spectra of observations A and B with the model TBabs * (varabs^{warm} * vpshock^{warm} + varabs^{hot} * vpshock^{hot}). Other parameters are separately shown in table 4.

* Abundance ratios by number are expressed relative to helium.

Errors and upper limits are at the 90% confidence level. The abundance of H was set to zero. We adopted the abundance ratio C/He = 0.4 by number, which was taken from Hillier & Miller (1999). The abundance of nickel is linked to that of iron.

^f Value fixed.

as ~ 21 eV.

3.3. Variable component

The emission from variable component constitutes a considerable fraction of the X-ray emission from WR 140 (see fig-

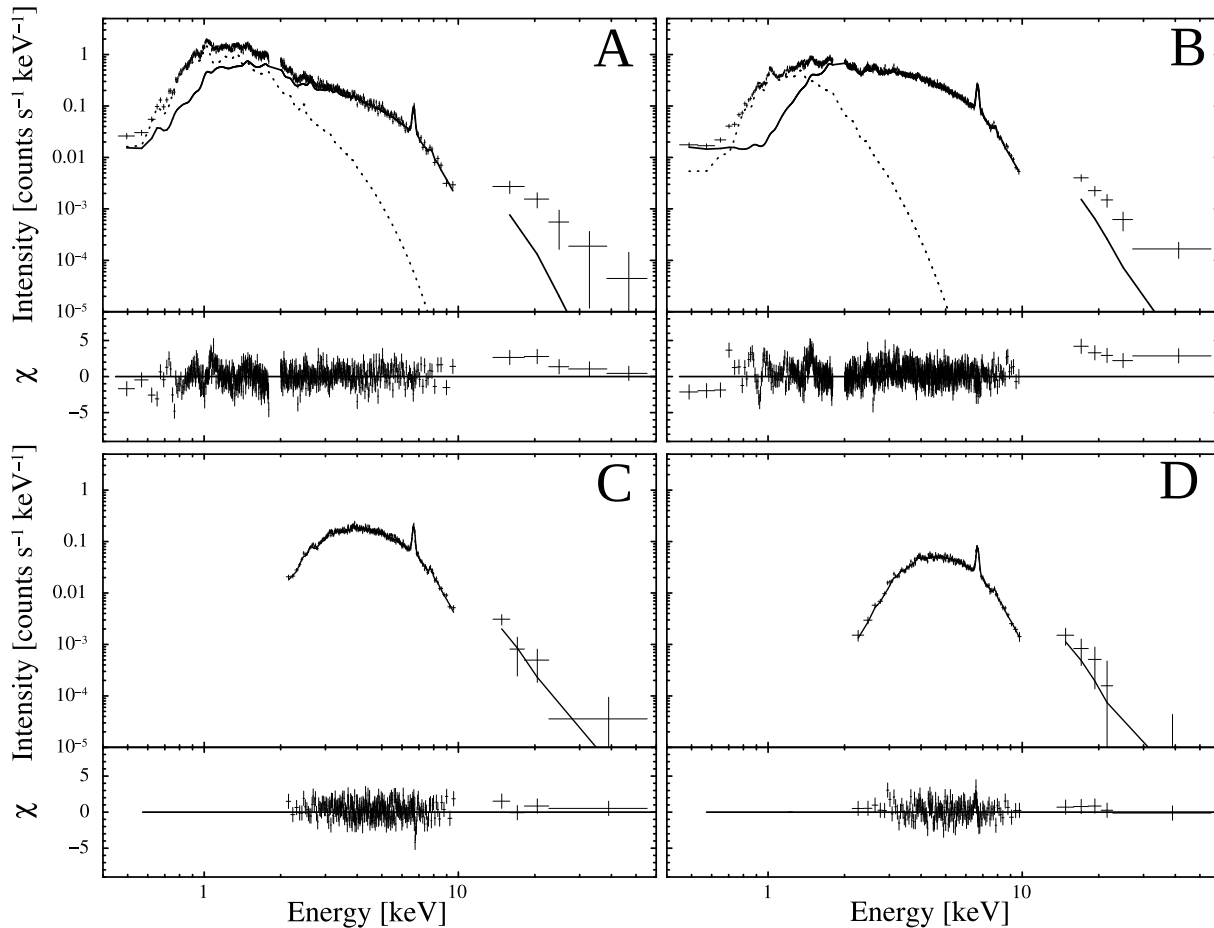


Fig. 9. The XIS/FI + HXD/PIN spectra of WR 140 for each observation and the XIS fitting models (see table 3 & 4). Backgrounds are subtracted. The hot and warm components are separately indicated as the solid and dotted lines in the upper panels. The lower panels show the residuals of the data from the best-fit model.

ure 3). For the spectral analysis, we then adopted the source and background regions used in § 3.1. As for observations C and D, we ignored the soft band below ~ 2 keV because there is the cool component (see figure 9).

3.3.1. Spectral fitting

In this subsection, we made the FI and BI spectra of observations A and B in the 0.5–10 keV band. We executed simultaneous fitting of the FI and BI spectra of observations A and B. We first tried to fit these spectra using a one-temperature plasma emission model with either a single absorption component or a combination of absorption components with two different optical depths. We next tried a two-temperature plasma emission model with a single common absorption. Both the attempts did not produce statistically acceptable solutions. This is perhaps because one-temperature plasma models do not reproduce emission lines in the soft band around 1 keV and iron K line at ~ 6.7 keV simultaneously, and those spectra, in particular in observation B, are too flat to be reproduced with a single absorption component.

We therefore fit the XIS spectra with a two-temperature (warm and hot) plasma model with independent absorption components (*varabs*)⁷. For the emission components, we

first used the CE plasma emission code, *vAPEC* (Smith et al. 2001) in which we can allow to vary each metal abundance. Next, we used the plane-parallel shock code, *vpshock*. In both of the fits, we fixed the C/He abundance ratio at 0.4 by number (Hillier & Miller 1999) and the other elements except for Ne, Mg, Fe and Ni at the best-fit abundances in Pollock et al. (2005). The latter fit gave slightly better reduced χ^2 values (2Tvapec: $\chi^2/\text{dof} \sim 1.71$, 2Tvps shock: $\chi^2/\text{dof} \sim 1.61$). The top panels in figure 9 show the best-fit 2Tvps shock models and the spectra. We use the *vpshock* model in the following analysis.

The X-ray emission should be absorbed both in the W-R wind and ISM. We therefore assume two absorption components. One is the absorption component (*varabs*) for the W-R wind, whose elemental abundances are tied to those of the plasma (*vpshock*) model. Another is an interstellar absorption component, with elemental abundances fixed at ISM abundances (*TBabs*: Wilms et al. 2000). We also assumed that the warm component in observation A suffers only interstellar absorption.

We tied elemental abundances of the both plasmas for observations A and B, since the elemental abundance of the plasma

⁷ We found that the line shift, which we will discuss in § 3.3.2, had little effect on the overall fit, so that we did not change the red-shift parameter in the spectral model.

⁷ We found that the line shift, which we will discuss in § 3.3.2, had little

Table 4. The best-fit parameters of spectral fitting for the variable components.

Observation	A	B	C	D
Orbital phase	2.904	2.989	2.997	3.000
interstellar absorption				
N_{H} (10^{21} cm $^{-2}$)	$8.51^{+0.05}_{-0.11}$	= A	= A (fixed)	= A (fixed)
warm component				
$N_{\text{He}}^{\text{warm}}$ (10^{19} cm $^{-2}$)	–	$4.35^{+0.07}_{-0.10}$	–	–
$k_{\text{B}}T^{\text{warm}}$ (keV)	$0.645^{+0.014}_{-0.006}$	$0.3515^{+0.0008}_{-0.0006}$	–	–
τ_{u}^* (10^{12} s cm $^{-3}$)	$8.2^{+2.5}_{-1.2}$	$4.1^{+1.1}_{-0.5}$	–	–
norm \dagger (10^{-3})	$9.97^{+0.04}_{-0.02}$	$14.4^{+0.3}_{-0.6}$	–	–
F_{X}^{\ddagger} (10^{-11} erg cm $^{-2}$ s $^{-1}$)	1.28	0.45	–	–
L_{X}^{\S} (10^{34} erg s $^{-1}$)	2.08	4.67	–	–
$L_{\text{X,bol}}^{\parallel}$ (10^{34} erg s $^{-1}$)	3.84	10.6	–	–
hot component				
$N_{\text{He}}^{\text{hot}}$ (10^{20} cm $^{-2}$)	≤ 0.007	$1.68^{+0.02}_{-0.03}$	12.6 ± 0.2	23.4 ± 0.5
$k_{\text{B}}T^{\text{hot}}$ (keV)	$3.29^{+0.06}_{-0.05}$	$3.48^{+0.04}_{-0.03}$	$2.97^{+0.07}_{-0.05}$	$3.03^{+0.08}_{-0.11}$
τ_{u}^* (10^{12} s cm $^{-3}$)	8.2#	4.1#	$2.7^{+1.9}_{-0.8}$	≥ 2.5
norm \dagger (10^{-2})	1.27 ± 0.01	$3.45^{+0.01}_{-0.02}$	$3.56^{+0.08}_{-0.10}$	$1.89^{+0.10}_{-0.08}$
F_{X}^{\ddagger} (10^{-11} erg cm $^{-2}$ s $^{-1}$)	2.85	5.63	2.58	1.01
L_{X}^{\S} (10^{34} erg s $^{-1}$)	1.67	5.10	5.78	2.51
$L_{\text{X,bol}}^{\parallel}$ (10^{34} erg s $^{-1}$)	2.59	9.08	11.7	4.13
χ^2/dof	3744/2330		556/472	297/253

Notes. For observations A and B, we adopted the model TBabs * (varabs^{warm} * vpshock^{warm} + varabs^{hot} * vpshock^{hot}). In observation A, we removed varabs^{warm} in order to determine the interstellar absorption for WR 140. On the other hand, for observations C and D, we adopted the model TBabs * varabs^{hot} * vpshock^{hot}. Errors and upper limits are at the 90% confidence level. The elemental abundance ratios of the variable components (warm and hot components) and the absorption components are separately shown in table 3.

* Ionization timescale

\dagger Normalization constant defined as $E.M. \times 10^{-14} (4\pi d^2)^{-1}$, where $E.M.$ is the emission measure in cm $^{-3}$ and d is the distance in cm.

\ddagger The absorbed flux (0.5–10 keV)

\S The absorption-corrected luminosity (0.5–50 keV), which we calculated by assuming a distance of 1.67 kpc.

\parallel The intrinsic bolometric luminosity

Ionization timescale of the hot component is tied to that of warm component.

should not change between observations A and B. We also tied the ionization parameters τ_{u} for both hot and warm components. The best-fit results are given in tables 3 and 4. The best-fit model for the spectrum of observation A gives an absorption column of $N_{\text{H}} = 8.51 \times 10^{21}$ cm $^{-2}$. The observation A is correspond to orbital phase = 2.904, in the definition of Monnier et al. (2011). The column density is close to that obtained with an earlier observation with *Chandra* ($N_{\text{H}} = 8.0 \times 10^{21}$ cm $^{-2}$ at orbital phase = 1.986; Pollock et al. 2005).

The interstellar extinction toward WR 140 has been measured at the optical wavelength as $A_V = 2.95$ mag (Morris et al. 1993). Based on the A_V , the expected ISM absorption column (N_{H}) is either 6.5×10^{21} (using the correlation of Gorenstein 1975) or 4.6×10^{21} cm $^{-2}$ (using the correlation of Vuong et al. 2003). In these correlations, we assumed that the gas-to-dust ratio of WR 140 is the same as that in ISM. The observed absorption at the phase A differs from the expected absorp-

tions only by a factor of two. The absorption appearing in the data of observation A may be mainly made by the ISM toward WR 140. For simplicity, we regard the X-ray absorption in the spectrum of observation A as the interstellar absorption hereafter. No conclusion in this paper changes with this simplification.

We fit the spectra of observations C and D independently. We executed simultaneous fitting of FI and BI spectra. Since the soft band flux below ~ 4 keV is strongly suppressed by circumstellar absorption, we did not include the warm component in the fits to either the spectrum of observation C or that of observation D. The elemental abundance were fixed at the best-fit values of observations A and B (see table 3). The bottom panels in figure 9 and table 4 show the best-fit results.

3.3.2. Fe K-line Profile

The XIS spectra showed emission lines of Fe xxv K α (~ 6.7 keV), Fe xxvi Ly α (~ 6.9 keV), Ni xxvii K α (~ 7.8 keV) and

Table 5. Results of spectral fitting in the 5–9 keV band.

Obs.	I.D.	A	B	C	D
Power-law					
Γ		3.0 ± 0.2	$2.98^{+0.07}_{-0.06}$	3.21 ± 0.08	$2.98^{+0.03}_{-0.05}$
norm*		0.04 ± 0.01	$0.12^{+0.02}_{-0.01}$	$0.17^{+0.03}_{-0.02}$	0.06 ± 0.01
Gaussian					
E_1^\dagger (eV)	FeXXV $K\alpha$	$6697 \pm 9 \pm 7$	$6678^{+3}_{-4} \pm 7$	$6668 \pm 4 \pm 7$	$6661^{+4}_{-5} \pm 7$
v^\ddagger (10^2 km s $^{-1}$)		$-8.6^{+4.2}_{-4.5} \pm 3.1$	$-0.9^{+1.8}_{-1.4} \pm 3.1$	$+4.5^{+2.5}_{-2.3} \pm 3.1$	$+7.7^{+3.1}_{-2.3} \pm 3.1$
σ_1 (eV)		< 5	< 19	< 15	< 31
F_1^\S		5.8 ± 0.6	18.1 ± 0.6	16.1 ± 0.6	9.4 ± 0.5
E_2 (eV)	FeXXVI $Ly\alpha$	6973^f	6973^f	6973^f	6973^f
F_2^\S		< 0.5	1.0 ± 0.4	0.51 ± 0.4	< 0.2
E_3 (eV)	NiXXVII $K\alpha$	7797^f	7797^f	7797^f	7797^f
F_3^\S		< 0.9	1.3 ± 0.6	1.1 ± 0.7	$0.9^{+0.3}_{-0.4}$
E_4 (eV)	FeXXV $K\beta$	7897^f	7897^f	7897^f	7897^f
F_4^\S		< 0.8	< 0.9	0.8 ± 0.7	< 0.3
χ^2/dof		128/96	278/238	192/158	151/159
Mn $K\alpha^\parallel$ (eV)		5904^{+5}_{-3}	5889^{+4}_{-2}	5896 ± 2	5898^{+1}_{-3}

Notes. Errors and upper limits are at the 90% confidence level. Subscript Numbers show

1=FeXXV $K\alpha$, 2=FeXXVI $Ly\alpha$, 3=NiXXVII $K\alpha$ and 4=FeXXV $K\beta$.

* Normalization constant, defined as the flux density at 1 keV in units of photons keV $^{-1}$ cm $^{-2}$ s $^{-1}$.

† The first and second errors show a statistical error and a systematic error, respectively.

‡ Line radial velocity. Relative velocities are based on the line center energy of FeXXV $K\alpha$ \sim 6,676 eV in the rest frame.

§ Line flux in 10^{-5} photon cm $^{-2}$ s $^{-1}$.

^f Line center values were fixed.

|| The center energy of Mn $K\alpha$ line from the ^{55}Fe calibration source.

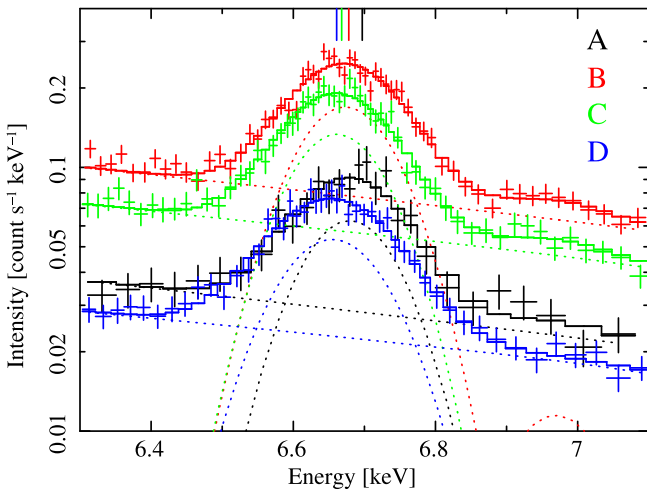


Fig. 10. The zoomed XIS/FI spectra of WR 140 for each observation and the fitting models (see table 5.) The black, red, green and blue show the observation A, B, C and D, respectively. The dotted lines show the power-law and Gaussian components. The solid lines show their summation. Vertical lines indicate the central energies of the FeXXV $K\alpha$ line for observations A, B, C and D.

FeXXV $K\beta$ (\sim 7.9 keV). In order to investigate the variation

of their line profiles, we measured the center energies, widths and fluxes of these lines using the FI data which has better gain calibration and higher sensitivity in the hard energy band. We fitted the spectra in the 5–9 keV band with a continuum model and four Gaussian models for the lines. For the continuum emission, we tried the two different models, thermal bremsstrahlung and power-law. Both fits gave consistent results. In fact, the best-fit parameters of the lines for two different continuum models are found to be within the margin of error. We therefore show only the best-fit parameters of a power-law model for the continuum and four Gaussian models for the lines. We fixed the line-center energies, except for that of FeXXV $K\alpha$ line, at the rest frame values, due to poor photon statistics. Figure 10 and table 5 show the best-fit results. The advantage of Suzaku-XIS is that the energy-scale is calibrated very well with the accuracy of roughly 0.1% (e.g., Koyama et al. 2007b; Ota et al. 2007; Ozawa et al. 2009; Tamura et al. 2011). Therefore, we adopted the systematic errors of 0.1% (7 eV) in our result, as are shown in table 5.

As the binary system approached periastron, the central energy of FeXXV $K\alpha$ line gradually shifted from $6,697 \pm 9$ eV (observation A) to $6,661^{+4}_{-5}$ eV (observation D). In order to measure the shift of the central energy of the FeXXV $K\alpha$ line, we determined the line center energy in the rest frame for the CE plasma model ($k_B T \sim 3$ keV). Here, we used the `fakeit`

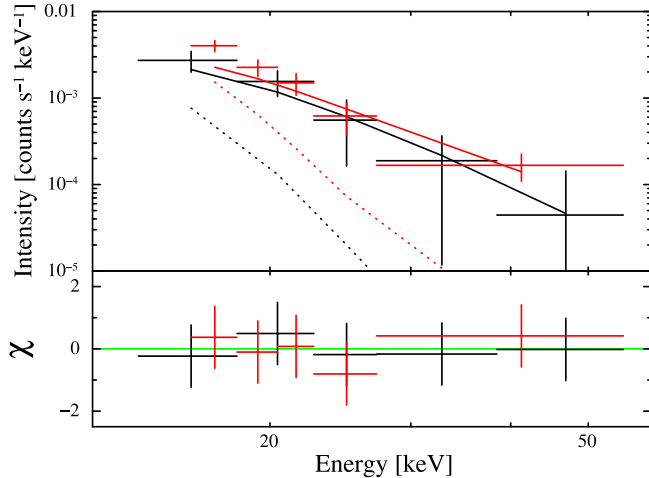


Fig. 11. The HXD/PIN spectra of WR 140 for observations A and B and the best-fit models. The black and red show observations A and B, respectively. The solid and dotted lines in the upper panel show the power-law and hot components, respectively. Lower panel shows the ratios of the data to the best-fit model. See also table 6.

of XSPEC to take account of the influences of not only dominant iron lines but also other weak lines derived from other elements. The line center energy was $\sim 6,676$ eV.

We have to pay attention to the fact that the line center energy could shift with variations of the flux ratios between the resonance, intercombination and forbidden lines, which are caused by non-equilibrium ionization. The ionization timescale τ_{ion} changed by a factor of three from observation A to D (see table 4). In order to check the influences of the difference of the ionization timescale, we estimated the center energies based on the *fakeit* with the non-equilibrium ionization models (table 4). The center energies for non-equilibrium ionization models had no difference and were exactly similar to that for the CE plasma model in the result. Therefore, we regarded the observed shifts in the line center energy as the Doppler shift.

The radial velocity changed from -860 to $+770$ km s^{-1} from observation A to that of D. The radial velocities in table 5 were calculated by adopting the rest frame energy as 6,676 eV. This is consistent with the earlier result of *Chandra* observations obtained by Pollock et al. (2005) (orbital phase = 1.986 and 2.032). They reported that Fe XXV line was shifted from -600 km s^{-1} to $+648 \pm 259$ km s^{-1} during the periastron passage. Such a variation was also seen in He I line in the near-infrared band during the periastron passage in 2001 (Varricatt et al. 2004). In addition, Marchenko et al. (2003) reported similar shifts of C III and He I lines at optical wavelength, which are thought to be emitted from wind-wind collision layer. Our observed variation of line center energy is consistent with such Doppler motions. This indicates that the emission in all wavelengths comes from a common shock cone.

Table 6. Results of spectral fitting in the 15–50 keV band.

Observation	A	B
Orbital phase	2.904	2.989
power-law component		
Γ	$1.7^{+1.1}_{-0.8}$	= A
norm * (10^{-3})	$1.5^{+36.8}_{-1.4}$	$1.8^{+51.0}_{-1.7}$
F_X^\dagger (10^{-12} erg cm^{-2} s^{-1})	7.3	9.0
L_X^\ddagger (10^{33} erg s^{-1})	6.2	7.6
χ^2/dof	1.34/7	

Notes. We adopted the model TBabs * (varabs^{warm} * vpshock^{warm}) + varabs^{hot} * (vpshock^{hot} + powerlaw). We fixed the warm and hot components at the best-fit values (see tables 3 and 4). Errors and upper limits are at the 90% confidence level. * Normalization constant of the power-law model defined as photons $\text{keV}^{-1} \text{cm}^{-2} \text{s}^{-1}$ at 1 keV.

† The absorbed flux (15–50 keV)

‡ The absorption-corrected luminosity (0.5–50 keV) was calculated assuming a distance of 1.67 kpc.

3.4. Hard excess above 10 keV

Figure 9 shows the XIS and HXD/PIN spectra and the XIS best-fit models of the variable component⁸. As explained in § 3.1, the combined spectra of NXB and CXB were used as the HXD/PIN background spectra. In both A and B observations, we found the hard-tail excess emission in the HXD/PIN band. The excess count rates after deduction of the emission from variable component at observations A and B are 0.022 and 0.021 counts per second in the 15–50 keV band, respectively. On the other hand, in observations C and D, there are no significant excess emission in the HXD/PIN band spectra.

Hereafter, we fit the excesses from the warm and hot components in observations A and B, respectively. We introduce a power-law model for the hard band excess. We simultaneously fit HXD/PIN spectra of observations A and B, tying the power-law index, since the HXD/PIN spectra are limited in photon statistics. Since the spectra do not constrain the soft band shape of the hard band excess, we assumed the same absorption to the excess component as that to the hot component in each phase. The best-fit model yields a power-law index $\Gamma = 1.7$. However, the hard band excess could be plausibly reproduced with a bremsstrahlung model with $k_B T > 10$ keV, too. The results are shown in figure 11 and table 6.

We have to consider the contamination from the other hard X-ray source IGR J20216+4359, because this source is located in the field of view of HXD/PIN. We discuss this contamination in detail in § 4.4.

4. Discussion

The warm, hot and hard band excess components vary with orbital phase. The cool component is detected only from obser-

⁸ Since the vpshock model does not cover the energy band above 10 keV, we used the vAPEC model to estimate the thermal contribution in the HXD energy range.

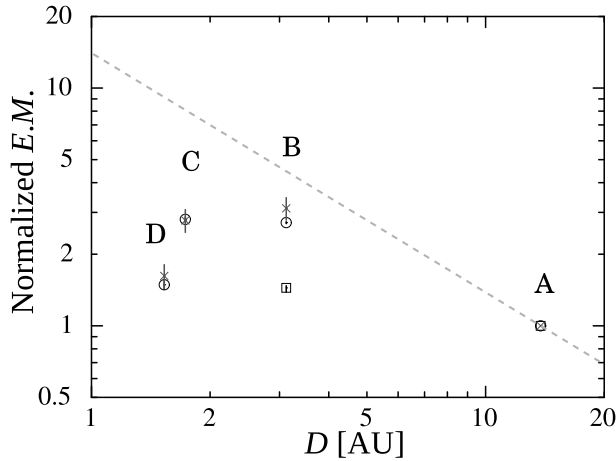


Fig. 12. The variation of the normalized emission measure and normalized line flux (\square warm component, \circ hot component, \times Fe line) with stellar separation. The dashed line shows an inverse proportion to the distance between the two stars.

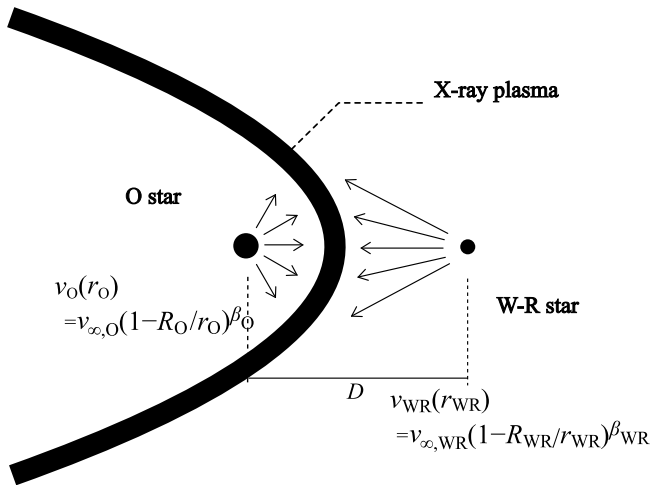


Fig. 13. A cartoon of a colliding-wind binary. D , r_O and r_{WR} show binary separation, the distance from the O star to the colliding-wind region and the distance from the W-R star to the colliding wind region, respectively.

observations C and D. The cool component appears nearly constant.

4.1. The nature of the cool component

The cool component was discovered for the first time with this observation. The simple analysis of one-temperature CE plasma emission for the cool component failed to reproduce the observed spectra with the residuals at 1.21 keV and other energies remaining in the spectral fitting. The energy of the residuals coincides fairly well with the free-bound absorption features of the highly ionized ions of O, Ne and Mg elements. The fit is then significantly improved with the recombining collisional plasma model, which introduces the radiative recombination continua (RRC).

The $\text{Ly}\beta/\text{Ly}\alpha$ line flux ratio of Ne in the cool component is also found to be significantly higher than that expected for the CE plasma (figure 8). The high flux ratio can be under-

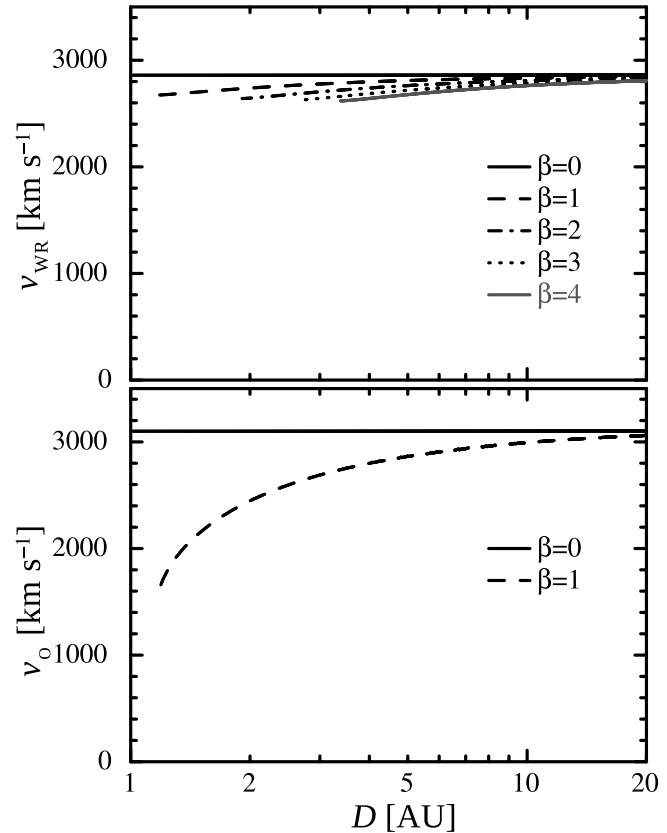


Fig. 14. The binary separation vs. wind velocity at the stagnation point. Top: W-R star. Bottom: O star.

stood with a transition process from a recombination of free electrons. Both the high $\text{Ly}\beta/\text{Ly}\alpha$ ratio and the RRC features indicate that the cool component is interpreted as a collisional plasma in a recombining phase.

The small absorption column of an order of $10^{21} \text{ H cm}^{-2}$ (see table 2) constrains the location of the cool component (figure 7). The spectra of the hot components are heavily absorbed below 1.6 keV at observations C and D. The large difference in the absorptions between both components indicates that the cool component is not deeply embedded in the wind-wind collision layer at observations C and D. Moreover, the column density for the cool component is similar to or is rather smaller than that for the warm and hot components at observation A, in which the distance of colliding wind region to the W-R star is about 10 AU. This suggests that the cool plasma is located far away from the W-R star by 10 AU or more.

In conclusion, the cool component that we discovered can be interpreted as a collisional plasma in a recombining phase. A potential scenario is as follows. The plasma was heated in the past by a wind-wind collision shock. The plasma then escaped from the dense wind region, and now, is recombining electrons and emitting the radiative recombination continuum along with the collisional plasma emission.

The initial temperature $k_B T_{\text{init}}^{\text{cool}}$ of the cool component was derived from the fitting results with the recombining collisional plasma model (table 2). The range of $k_B T_{\text{init}}^{\text{cool}}$ contains the temperature of the warm and hot components, which were formed

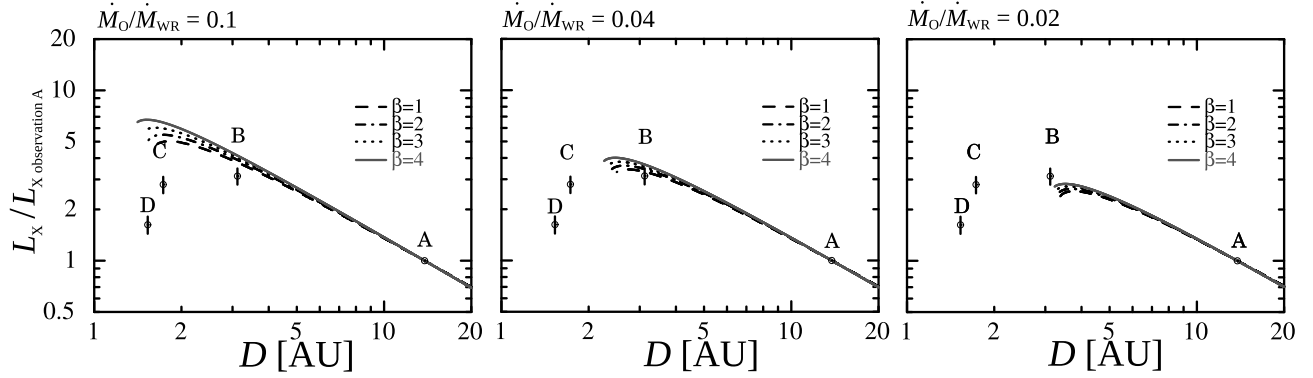


Fig. 15. Binary separation vs. normalized X-ray luminosity. The luminosity is normalized at the separation of observation A. \dot{M}_O/\dot{M}_{WR} in the left, center and bottom panels are 0.1, 0.04 and 0.02, respectively. The β_O for the O star is fixed to be unity. The lines show the equation (1).

by the wind-wind collision. On the one hand, the plasma temperature $k_B T^{\text{cool}}$ is now 0.021 keV (table 2). This temperature of the cool component is between the temperature of the wind-wind collision plasma and that of the dust detected in the infrared wavelengths (Williams et al. 2009). The observed cool component might be emitted from the area in a *transition* phase, where the hot gas, compressed by the wind-wind collision, is cooling down and is forming dust.

The cooling of the shock heated plasma in wind-wind collision layer should be common in all the W-R binaries. If so, is the recombining plasma with less absorption detected commonly in them? The RRC structures in the X-ray spectra were reported from the two bright colliding wind binaries γ^2 Velorum (WC8 + O7.5; Schild et al. 2004) and θ Muscae (WC5 + O6 + O9.5; Sugawara et al. 2008). At least, the emission component with the RRC structure of γ^2 Velorum is less absorbed. γ^2 Velorum and θ Muscae are both WC-subtype W-R binaries. On the other hand, no detection of the RRC structure was reported from the other subtype WN. Systematic and deep search of the structure from W-R binaries is critical to answer the question.

4.2. Flux variation of the hot component

From table 4, we can see that the emission measure of the hot component varied. Generally, in colliding wind binaries, the emission measure in colliding wind region is expected to vary along with inversely proportional relation with the binary separation D (Usov 1992). In order to check whether WR 140 varied with this relation, we plotted the emission measure of the hot component in figure 12. The emission measure of the warm component and Fe XXV $K\alpha$ line flux are also plotted in the same figure. As the phase approaches toward periastron, to observation C and then to D, the emission measure of the hot component deviated from the expected $1/D$ law. No numerical simulation ever published predicts a rapid flux decrease at periastron, although some theorists simulated the variation of the X-ray luminosity for the colliding-wind binary (e.g., Luo et al. 1990; Stevens et al. 1992; Myasnikov & Zhekov 1993).

We therefore took account of not only the separation D , but also another parameter. According to the equation (10) in Stevens et al. (1992), the intrinsic X-ray luminosity of the colliding wind zone can be written as

$$L_X \propto D^{-1}(1+A)/A^4, \quad (1)$$

where the wind momentum flux ratio, $A = ((\dot{M}_{WR} v_{WR}(r_{WR})) / (\dot{M}_O v_O(r_O)))^{1/2}$. Here, r_O and r_{WR} show the distances to the shock region from the O star and from the W-R star, respectively. The geometry is sketched in figure 13. Note that A is not constant and changes depending on not only the binary separation D but also the wind acceleration parameter β and the ratio of mass-loss rates.

At periastron, the momentum flux of the O-type wind should become significantly smaller, since its wind has less space to reach terminal velocity before entering the shock region, while the W-R wind should be less affected. In figure 14, we show the maximum pre-shock stellar wind velocities of the W-R and O stars at a given binary separation. We adopted a simple beta law for the wind acceleration: $v(r) = v_\infty(1 - R/r)^\beta$. Here, v_∞ and R are the terminal wind velocity and the stellar radius, respectively. We used the value of $v_{\infty,WR} = 2860 \text{ km s}^{-1}$ (Williams et al. 1990), $v_{\infty,O} = 3100 \text{ km s}^{-1}$ (Setia Gunawan et al. 2001), $R_{WR} = 2 R_\odot$ and $R_O = 26 R_\odot$ (cf. Williams et al. 2009). Many studies (e.g., Puls et al. 1996; Lépine & Moffat 1999) indicate that the β value of O star winds should be near 1, while W-R stars can have larger values $\beta > 1$. We therefore fixed the β value of O star wind to unity in the following simulations. The actual β value for the W-R star is not so important since the stagnation point is far from the W-R star. Near the shock region, the W-R wind reaches its terminal velocity for any assumed β , while the O-star wind lags far behind. As a result, the wind momentum flux ratio, A , rapidly becomes large near periastron. This means that the stagnation point approaches the O star.

In figure 15, we plot the normalized X-ray luminosity as a function of the binary separation D . The luminosity is normalized at the separation of observation A ($D \sim 14 \text{ AU}$). In this figure, we adopted the X-ray luminosity ratio of the hot components. The bolometric X-ray luminosity ratio of the warm component to the hot one is about one in observations A and B (table 4). We assumed that the ratios in observations C and D remain unchanged. The observed luminosity peak appears near observation B. The luminosity drops at observations C and D and indicates the wind momentum ratio cannot be constant; $\beta \neq 0$.

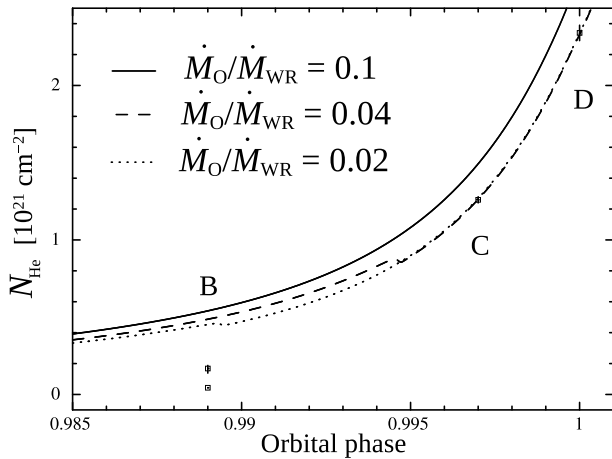


Fig. 16. The helium column density for the warm and hot components plotted against the orbital phase. Observed absorptions are plotted by a bar and the calculated absorption by solid lines. In this plot, we assumed $\dot{M}_{\text{WR}} = 2.2 \times 10^{-5} M_{\odot} \text{yr}^{-1}$, $\beta_{\text{WR}} = 1$ and $\beta_{\text{O}} = 1$.

We calculate equation (1) for three assumptions of the mass-loss rate ratio $\dot{M}_{\text{O}}/\dot{M}_{\text{WR}} = 0.1, 0.04,$ and 0.02 . The β model can reproduce the luminosity during observations A and B. However, it is truncated near periastron for all the assumptions since the wind momentum of the W-R star overwhelms that of the O star. This implies that the stagnation point almost arrives at the surface of the O star near observations C and D. The observed (intrinsic, absorption-free) X-ray luminosity during observations C and D is then mostly produced near the surface of the O star.

One may think the radiative inhibition because of the stronger radiation field of the O star (radiative braking effect: Stevens & Pollock 1994). Setia Gunawan et al. (2001) took the “eclipse spectra” ratio of the IUE spectrum very close to periastron (phase 0.01) to a composite from phases 0.5 to 0.95 (figure 7 in Setia Gunawan et al. 2001). The spectra shows red-shifted absorption at 1300 km s^{-1} in the Si IV 1394–1403 doublet and 1400 km s^{-1} in the C IV 1548–1551 doublet. At this phase the O star behind the W-R star was seen and the W-R wind was being looked through towards the stagnation point. By correcting the velocity with the inclination of 54 degrees, the wind velocity was radiatively braked and was estimated as about 2300 km s^{-1} before the collision with the O star wind, i.e. about 80% of its terminal velocity when it meets the O stellar wind.

If the radiation breaking dominates the momentum balance in the collision layer, the WC star winds lose its momentum and the cone angle of the collision layer will be enlarged, making the X-ray luminosity increased. The observed flux drop at the periastron indicates that the radiative wind breaking is not a major effect to control the momentum balance in the wind-wind collision layer (i.e., X-ray luminosity).

In this condition, the mass-loss ratio $\dot{M}_{\text{O}}/\dot{M}_{\text{WR}}$ of 0.04 is good to explain the observed luminosities at observation B. If we adopted this mass-loss ratio and $\dot{M}_{\text{WR}} \sim 2.2 \times 10^{-5} M_{\odot} \text{yr}^{-1}$, which reproduced the observed column densities at observations C and D (for the detail, refer to § 4.3), we obtain $\dot{M}_{\text{O}} \sim 9 \times 10^{-7} M_{\odot} \text{yr}^{-1}$. This mass-loss rate for

the O star is close to that recently reported by a number of analyses ($\dot{M}_{\text{O}} = 8 \times 10^{-7} M_{\odot} \text{yr}^{-1}$; Pittard & Dougherty 2006, $\dot{M}_{\text{O}} = 1 \times 10^{-6} M_{\odot} \text{yr}^{-1}$; Fahed et al. 2011).

4.3. Estimation of the W-R mass-loss rate

We estimated the mass-loss rate of the W-R star from the observed column density N_{He} . The mass-loss rate for a spherically symmetric wind is expressed as $\dot{M}_{\text{WR}} = 4\pi r^2 \rho(r) v_{\text{WR}}(r)$, in which r is the distance from the center of the W-R star. Here, ρ is the wind mass density. In addition the He-equivalent column density can be expressed as $N_{\text{He}} = \int \rho(r) dl \times \alpha / 4m_{\text{p}}$ from the X-ray emitting region to infinite distance along the line of sight “ l ” (cf. Williams et al. 1990). Here, m_{p} is the proton mass and α is the ratio of helium mass to total mass in the W-R wind. We therefore apply for the mass-loss rate of the W-R star, whose column density gives close agreement with the observed He-equivalent column density.

The computed He-equivalent column density was obtained as follows. We first calculated the stagnation point in consideration of the effect of non-constant wind momenta, as shown in § 4.2. Then, we assumed that the X-ray is emitted from the stagnation point. Finally, we calculated the absorption column density of the W-R stellar wind. Here, we used $\alpha = 0.4$, which was calculated by utilizing the elemental abundances of table 3. We adopted a simple beta law model for the wind acceleration: $v(r) = v_{\infty} (1 - R/r)^{\beta}$. We used the same values of v_{∞} , R and β for the W-R and O stars as those in § 4.2. An orbital inclination angle $i = 120^{\circ}$ was adopted (Dougherty et al. 2005).

Figure 16 shows a plot of the best-fit column density from table 4. We also plotted our calculated column density through the W-R wind, in the case of $\dot{M}_{\text{WR}} \sim 2.2 \times 10^{-5} M_{\odot} \text{yr}^{-1}$. Here, we tested the three cases with the mass-loss rate ratios of $\dot{M}_{\text{O}}/\dot{M}_{\text{WR}} = 0.1, 0.04,$ and 0.02 . The calculated column densities for the $\beta_{\text{WR}} = 1, 3$ and 5 were much the same. In observation A, we set the absorption column density caused by the W-R wind to zero. The absorption column density by the wind increased as the binary approached periastron. In the case of $\dot{M}_{\text{O}}/\dot{M}_{\text{WR}} = 0.04,$ and 0.02 , the stagnation points at observations C and D were at the O star surface.

We assumed that the wind-wind collision layer is concentrated in a small region at the stagnation point. The good correspondence between the model and the data, in observations C and D, indicates our assumption is reasonable at least in the phases. On the other hand, at observation B, there is a discrepancy by a factor of two between the data and the model. The layer at observation B is largely extended away from the stagnation point and the O star. During observation B, the X-rays emitted from the wind-wind collision layer will suffer absorption at different column density according to the different line of sight.

In the calculation of the wind absorption, we assumed values for the stellar radius of the W-R star R_{WR} , the inclination angle i of the binary system and the C/He abundance ratio. If the stellar radius of the W-R star was in fact, for example, a half of our assumed value, i.e., $R_{\text{WR}} = 1 R_{\odot}$, the absorption column at periastron would be lower by roughly 10% than the above-mentioned value. If the inclination angle was a five-degree larger than our assumed value, the absorption column

at periastron would be larger by roughly 10%. If the assumed C/He abundance ratio was a half of it, i.e., $C/He = 0.2$, the absorption column at periastron would be larger by roughly 20%. Or, if the ratio was doubled, i.e., $C/He = 0.8$, the column at periastron would be 20% lower. As such these three parameters are sensitive to N_{He} . Accordingly the mass-loss rate derived from N_{He} may have some considerable uncertainty.

Williams et al. (1990) derived the mass-loss rate $\dot{M}_{WR} \sim 5.7 \times 10^{-5} M_{\odot} \text{ yr}^{-1}$, which assumed a distance of 1.3 kpc and made no allowance for clumping, from the radio flux at the quiescent phase. Allowing for the clumping having a filling factor of 0.1 and the revised distance, the mass-loss rate \dot{M}_{WR} was determined as $2.6 \times 10^{-5} M_{\odot} \text{ yr}^{-1}$. By using X-ray absorption, we obtained $\dot{M}_{WR} \sim 2.2 \times 10^{-5} M_{\odot} \text{ yr}^{-1}$ at observations C and D near the periastron. Our value can coincide with that by using the radio flux.

4.4. Upper limit of the hard band excess

We have detected a signal in the high-energy band above 10 keV (figure 9). However, the Seyfert 2 Galaxy, IGR J20216+4359, is located in the field of view of PIN/HXD. The detected hard-tail signal may be contaminated with the emission from IGR J20216+4359.

IGR J20216+4359 was discovered by Bikmaev et al. (2008) during their eleven months observation. According to Bikmaev et al. (2008), IGR J20216+4359 is highly absorbed ($N_H = 1.3 \times 10^{23} \text{ cm}^{-2}$), when they fixed Γ to 1.7, which is a typical value of a Seyfert 2 Galaxy. By assuming the flux and the spectral shape are the same as those in Bikmaev et al. (2008) through our observations, we estimated the count rate of the contamination from IGR J20216+4359. The model predicted count rate with HXD/PIN is dependent on the off-axis angle of IGR J20216+4359. The count rates at observations A, B, C and D are 0.013, 0.017, 0.016 and 0.016 counts per second in the 15–50 keV band, respectively. The contaminations from IGR J20216+4359 accounts for about 60 and 80% of the excess count rates at observations A and B, respectively. On the other hand, there are no excess count rates at observations C and D. The count rates from off-axis IGR J20216+4359 at observations C and D were 2.0 and 3.2 times larger than the observed count rates in the 15–50 keV band, respectively. This suggests that the flux of IGR J20216+4359 were varied. Since the flux of IGR J20216+4359 was varied, we cannot constrain the origin of the hard band excess in observations A and B. Therefore, we regard the flux detected at observation B is an upper limit of the hard band excess from WR 140 ($L_X < 8 \times 10^{33} \text{ erg s}^{-1}$, see table 6). *ASTRO-H* and *NuSTAR*, which have hard X-ray imaging instruments with high sensitivity, will be useful to verify the existence of the hard band excess.

In the colliding-wind region, first-order diffusive shock acceleration results in the production of a power-law spectrum with index 2 for electrons (e.g., Bell 1978, Pollock 1987, Eichler & Usov 1993 and White & Chen 1995). The best-fit photon index ($\Gamma \sim 1.7$) indeed approximates a photon index for non-thermal electron energy distribution. Pittard & Dougherty (2006) discuss the photon index of the non-thermal emission from WR 140. They expected that the photon index is 1.7 above the energy of 1 MeV. Our fitting results are consistent with it, although our results have a large er-

ror. According to White & Chen (1995), the luminosity ratio of inverse Compton to synchrotron radiation can be written as $L_{syn}/L_{IC} = 840B^2r_O^2/L_O$, where the magnetic field B is expressed in G, r_O is the distance from the colliding-wind zone to the O star in AU, and L_O is the O star luminosity in L_{\odot} units. For example, during observation B, if we suppose $L_{IC} < 1 \times 10^{34} \text{ erg s}^{-1}$ (see table 6), $L_{syn} = 4.6 \times 10^{29} \text{ erg s}^{-1}$ for a distance of 1.67 kpc (phase=0.93; Dougherty et al. 2005), $L_O = 5.7 \times 10^{39} \text{ erg s}^{-1}$ (Dougherty et al. 2005), and $r_O \sim 0.3 \text{ AU}$, the total value of the magnetic field for observation B is $B > 1 \text{ G}$. Because of the difficulty of measuring the magnetic field of the W-R stellar surface, the value of the magnetic field around the W-R star will be helpful to study the evolution of the massive star.

5. Summary

We have observed the colliding-wind binary WR 140 around the 2009 periastron passage with the *Suzaku* satellite. The following are the salient results.

- A. We discovered a cool component. The absorption to this component is smaller than that to the other components. We infer that this component extends out farther than the other components does. Arguably this component may represent a transitional phase from the compressed hot gas to dust formation.
- B. The luminosity of the hot component is not inversely proportional to the binary separation. This discrepancy may be explained if the O-star wind collides with the W-R star wind before it has reached its terminal velocity, leading to a reduction in its wind momentum flux. This interpretation needs to be verified by future theoretical modelings.
- C. As WR 140 approaches periastron, the column density of the hot component increases. The column densities at near periastron are reproduced well with a simple model, in which the absorption is occurred in the W-R wind and the X-ray emitting region is fairly compact.
- D. We detected a hard X-ray signal above 10 keV in the HXD/PIN data. However, we could not eliminate the possibility of contamination from the background source IGR J20216+4359, 17.3 arcmin north-east of WR 140. The PIN data gives the upper-limit for the X-ray luminosity of WR 140, $8 \times 10^{33} \text{ erg s}^{-1}$.

We thank the referee for their help in improving the quality of this paper. We also thank M. Sakano for his invaluable help. This research has made use of data and/or software provided by the High Energy Astrophysics Science Archive Research Center (HEASARC), which is a service of the Astrophysics Science Division at NASA/GSFC and the High Energy Astrophysics Division of the Smithsonian Astrophysical Observatory. Y.S. acknowledges financial support from the Japan Society for the Promotion of Science. Y.T. and Y.M. acknowledge support from the Grants-in-Aid for Scientific Research (numbers 20540237, 21018009 and 23540280) by the Ministry of Education, Culture, Sports, Science and Technology. K.H. is grateful for financial support by the NASA's Astrobiology Institute (RTOP 344-53-51)

to the Goddard Center for Astrobiology. A. F. J. M. is grateful for financial aid to NSERC (Canada) and FQRNT (Québec). P. M. W. is grateful to the Institute for Astronomy for continued hospitality and access to the facilities of the Royal Observatory. J. M. P. would like to thank the Royal Society for funding a University Research Fellowship. This research has made use of NASA's Astrophysics Data System.

References

- Antokhin, I. I., Owocki, S. P., & Brown, J. C. 2004, *ApJ*, 611, 434
- Bell, A. R. 1978, *MNRAS*, 182, 147
- Bikmaev, I. F., Burenin, R. A., Revnivtsev, M. G., et al. 2008, *Astronomy Letters*, 34, 653
- Boldt, E. 1987, *Observational Cosmology*, 124, 611
- Corcoran, M. F., Pollock, A. M. T., Hamaguchi, K., & Russell, C. 2011, arXiv:1101.1422
- De Becker, M., Pittard, J. M., Williams, P., & WR 140 Consortium 2011, *Bulletin de la Societe Royale des Sciences de Liege*, 80, 653
- Dougherty, S. M., Beasley, A. J., Claussen, M. J., Zauderer, B. A., & Bolingbroke, N. J. 2005, *ApJ*, 623, 447
- Eichler, D., & Usov, V. 1993, *ApJ*, 402, 271
- Fahed, R., et al. 2011, *MNRAS*, 418, 2
- Fukazawa, Y., et al. 2009, *PASJ*, 61, 17
- Gorenstein, P. 1975, *ApJ*, 198, 95
- Hamaguchi, K., et al. 2007, *ApJ*, 663, 522
- Hillier, D. J., & Miller, D. L. 1999, *ApJ*, 519, 354
- Ishisaki, Y., et al. 2007, *PASJ*, 59, 113
- Kokubun, M., et al. 2007, *PASJ*, 59, S53
- Koyama, K., Kawada, M., Takano, S., & Ikeuchi, S. 1990, *PASJ*, 42, L1
- Koyama, K., Maeda, Y., Tsuru, T., Nagase, F., & Skinner, S. 1994, *PASJ*, 46, L93
- Koyama, K., et al. 2007, *PASJ*, 59, S23
- Koyama, K., Hyodo, Y., Inui, T., et al. 2007, *PASJ*, 59, 245
- Lépine, S., & Moffat, A. F. J. 1999, *ApJ*, 514, 909
- Luo, D., McCray, R., & Mac Low, M.-M. 1990, *ApJ*, 362, 267
- Maeda, Y., Koyama, K., Yokogawa, J., & Skinner, S. 1999, *ApJ*, 510, 967
- Marchenko, S. V., et al. 2003, *ApJ*, 596, 1295
- Mitsuda, K., et al. 2007, *PASJ*, 59, S1
- Monnier, J. D., Zhao, M., Pedretti, E., et al. 2011, *ApJL*, 742, L1
- Morris, P. W., Brownsberger, K. R., Conti, P. S., Massey, P., & Vacca, W. D. 1993, *ApJ*, 412, 324
- Myasnikov, A. V., & Zhekov, S. A. 1993, *MNRAS*, 260, 221
- Nugis, T., Crowther, P. A., & Willis, A. J. 1998, *A&A*, 333, 956
- Oskinova, L. M. 2005, *MNRAS*, 361, 679
- Ota, N., Fukazawa, Y., Fabian, A. C., et al. 2007, *PASJ*, 59, 351
- Ozawa, M., Uchiyama, H., Matsumoto, H., et al. 2009, *PASJ*, 61, 1
- Pittard, J. M., & Dougherty, S. M. 2006, *MNRAS*, 372, 801
- Pollock, A. M. T. 1987, *A&A*, 171, 135
- Pollock, A. M. T., Haberl, F., & Corcoran, M. F. 1995, *Wolf-Rayet Stars: Binaries; Colliding Winds; Evolution*, 163, 512
- Pollock, A. M. T., Corcoran, M. F., & Stevens, I. R. 2002, *Interacting Winds from Massive Stars*, 260, 537
- Pollock, A. M. T., Corcoran, M. F., Stevens, I. R., & Williams, P. M. 2005, *ApJ*, 629, 482
- Protassov, R., van Dyk, D. A., Connors, A., Kashyap, V. L., & Siemiginowska, A. 2002, *ApJ*, 571, 545
- Puls, J., Kudritzki, R.-P., Herrero, A., et al. 1996, *A&A*, 305, 171
- Puls, J., Markova, N., Scuderi, S., et al. 2006, *A&A*, 454, 625
- Schild, H., et al. 2004, *A&A*, 422, 177
- Serlemitsos, P. J., et al. 2007, *PASJ*, 59, S9
- Setia Gunawan, D. Y. A., van der Hucht, K. A., Williams, P. M., et al. 2001, *A&A*, 376, 460
- Schild, H., Güdel, M., Mewe, R., et al. 2004, *A&A*, 422, 177
- Smith, R. K., Brickhouse, N. S., Liedahl, D. A., & Raymond, J. C. 2001, *ApJL*, 556, L91
- Stevens, I. R. 1993, *MNRAS*, 265, 601
- Stevens, I. R., Blondin, J. M., & Pollock, A. M. T. 1992, *ApJ*, 386, 265
- Stevens, I. R., & Pollock, A. M. T. 1994, *MNRAS*, 269, 226
- Sugawara, Y., Tsuboi, Y., & Maeda, Y. 2008, *A&A*, 490, 259
- Takahashi, T., et al. 2007, *PASJ*, 59, S35
- Tamura, T., Hayashida, K., Ueda, S., & Nagai, M. 2011, *PASJ*, 63, 1009
- Usov, V. V. 1991, *MNRAS*, 252, 49
- Usov, V. V. 1992, *ApJ*, 389, 635
- Varricatt, W. P., Williams, P. M., & Ashok, N. M. 2004, *MNRAS*, 351, 1307
- Vuong, M. H., Montmerle, T., Grosso, N., et al. 2003, *A&A*, 408, 581
- White, R. L., & Becker, R. H. 1995, *ApJ*, 451, 352
- White, R. L., & Chen, W. 1995, *Wolf-Rayet Stars: Binaries; Colliding Winds; Evolution*, 163, 438
- Williams, P. M., van der Hucht, K. A., Pollock, A. M. T., Florkowski, D. R., van der Woerd, H., & Wamsteker, W. M. 1990, *MNRAS*, 243, 662
- Williams, P. M., et al. 2009, *MNRAS*, 395, 1749
- Wilms, J., Allen, A., & McCray, R. 2000, *ApJ*, 542, 914
- Zhekov, S. A., & Skinner, S. L. 2000, *ApJ*, 538, 808